



Adjusting inter-semiconductor barrier height via crystal plane engineering: Crystalline face exposed single crystal cadmium sulfide augmentative S-scheme heterojunctions for efficiently photocatalytic hydrogen production

Xuanpu Wang, Zhiliang Jin ^{*}

School of Chemistry and Chemical Engineering, Ningxia Key Laboratory of Solar Chemical Conversion Technology, Key Laboratory for Chemical Engineering and Technology, State Ethnic Affairs Commission, North Minzu University, Yinchuan 750021, PR China

ARTICLE INFO

Keywords:

Single crystal CdS
Active crystal plane
Photocatalytic hydrogen evolution
S-scheme heterojunction
DFT calculation

ABSTRACT

The design of crystalline face engineered photocatalysts can modulate the catalytic activity at the microscopic scale. The exposure ratio of (100), (002) and (101) crystal planes of CdS with visible light activity was adjusted by crystal plane engineering. Density functional theory (DFT) calculations and experiments show that the fully exposed (002) surface CdS-L (Leaf-like CdS) has excellent hydrogen evolution activity. The use of the interface heterojunction strategy can greatly mobilize the electron flow between CdS-L and CoS₂ S-scheme heterojunction compound semiconductors by changing the potential barrier difference. The CoS₂/CdS-L composite photocatalyst exhibits amazing hydrogen evolution activity under 5 W white light irradiation, and the hydrogen production rate can reach 19.22 mmol·g⁻¹·h⁻¹. The results of in situ radiation XPS tests and comparative experiments show that the catalysts with more exposed crystal planes on the basis of constructing S-scheme heterojunctions can provide more active sites and have stronger reactivity. The use of crystal facet engineering effect and interfacial heterojunction strategy lays the foundation for the structural design and large-scale application of highly active visible light catalysts.

1. Introduction

As fossil fuels continue to be depleted and global pollution increases dramatically, the search for a sustainable energy source for the future is the primary goal of human civilisation as it enters the next phase [1–3]. Water is the source of everything, and the ocean covers about 71 % of the world. The utilization of infinite solar energy to drive the decomposition of water into hydrogen, as an energy source, aligns with the future development trend [4,5], and it realizes the whole process of green, clean and sustainable from production to application [6,7]. In the process of theoretical exploration, the search for efficient photocatalysts is the primary goal toward industrialization. Efficient photogenerated carrier separation efficiency, fast electron leap, strong reduction ability, and high light absorption performance are all issues to be considered in the development of efficient photocatalysts [8,9].

Among the many known semiconductors, CdS is a highly active photocatalyst. There are many reports on enhancing the photocatalytic

activity of CdS [10,11]. For example, the design of nano-sized CdS through morphology modulation offers structural advantages that can significantly reduce the migration distance of photogenerated carriers and increase the specific surface area of the catalyst. This, in turn, enhances the fast charge transfer ability and exposes more active sites, effectively promoting the photocatalytic hydrogen evolution process [12,13]. In addition to the modulation of its own electronic structure and intrinsic properties, the introduction of other active substances to promote the photocatalytic performance of CdS can be considered, such as elemental doping, loading of co-catalysts, and the construction of heterojunctions [14]. It has been demonstrated that different crystallographic facets of the crystals exhibit differences in activity. By exploring and effectively the highly active facets will improve the catalyst performance in terms of molecular growth dimension [15]. According to previous studies, CdS (002) crystalline faces have the highest intrinsic activity, since the catalytic activity of semiconductor photocatalysts depends on their surface electronic and atomic structures [16], which in

^{*} Corresponding author.

E-mail address: zl-jin@nwnu.edu.cn (Z. Jin).

<https://doi.org/10.1016/j.apcatb.2023.123373>

Received 3 June 2023; Received in revised form 4 October 2023; Accepted 6 October 2023

Available online 8 October 2023

0926-3373/© 2023 Elsevier B.V. All rights reserved.

turn are strongly dependent on the crystal level. Therefore, this study is dedicated to explore the design and synthesis of highly active CdS (002) photocatalysts from theory to experiment [17].

The arrangement of atoms fundamentally determines the properties of the material. The particles within the crystal are arranged regularly and periodically in three-dimensional space, and the mass distribution throughout the crystal exhibits long-range ordered, which is a single crystal. Single crystals are usually characterized by a regular geometric shape, and homogeneity and anisotropy are inherent properties. In contrast, polycrystals are composed of many individual grains, and there is no regular arrangement between grains. In catalytic reactions, single crystal materials have great potential for application [18]. They possess inherent periodic pore channels that offer anisotropic sites for catalytic reactions to occur with specificity. The anisotropic environment provides additional selectivity for the occurrence of the reaction. Semiconductor mesoporous single crystal materials possess the high specific surface area, loading capacity, and mass transfer capability of porous materials, as well as the excellent charge transfer capability, catalytic activity, and chemical stability of single crystals [19]. Therefore, the exposure of highly active crystalline surfaces is regulated on the crystal to maximize catalytic activity, as the macroscopic properties of the internal parts remain unchanged.

Incorporating precious metals such as Pt, Au and Pd onto the photocatalytic surface will can significantly enhance catalytic activity [20], however, cost remains the primary consideration in catalyst design for industrial applications. Although CoS₂ possesses excellent metallic properties and intrinsic activity, its nano size inevitably leads to aggregation during synthesis. By loading it onto the CdS surface it can improve its agglomeration effect ensuring more active sites are exposed and also act as an electron collector instead of noble metals to build heterojunction [21]. This noble metal-free co-catalyst research is expected to address the cost issues in photocatalyst design.

In the present work, the exposure of highly active (002) crystal faces was achieved by modulating the CdS cell growth mechanism from. The construction of S-scheme heterojunctions between metallic CoS₂ and CdS achieves excellent photocatalytic hydrogen precipitation activity, and the formation of different barrier heights between different CdS leads to differences in their activity. Under 5 W white light irradiation, the hydrogen production rate of CdS-L reached 6 mmol·g⁻¹·h⁻¹, which was 3.5 and 1.9 times higher than that of CdS-R and CdS-P respectively, while the hydrogen precipitation rate of 15CC-L reached 19.22 mmol·g⁻¹·h⁻¹.

2. Experiments

2.1. Preparation of CdS

By changing the sulfur source and solvent, the growth of CdS cells in different spatial dimensions is realized to induce the ideal crystal surface exposure. Preparation of rod-like cadmium sulfide (CdS-R) [22,23]: cadmium nitrate and thiourea with molar ratio of 1:3 were added to 60 mL ethylenediamine, and the mixed solution was dissolved by sufficient agitation and reacted for 24 h at a temperature of 160 °C. CdS-R was obtained by washing the product with deionized water and ethanol for several times. Preparation of particle cadmium sulfide (CdS-P) [24]: 0.28 M cadmium nitrate and sodium sulfide hydrate solution were prepared respectively, then the sodium sulfide solution was slowly added to the cadmium nitrate solution, and the mixed solution reacted at 180 °C for 24 h. The product was washed with deionized water and ethanol to obtain CdS-P. Preparation of leaf-like cadmium sulfide (CdS-L) [25]: 1 mmol cadmium acetate and slightly excessive thiourea were added to 80 mL deionized water, and 0.8 mL hydrofluoric acid was added to the mixed solution after stirring and dissolving. After 60 min stirring, the reaction was carried out at 200 °C for 20 h. The product was washed with deionized water and ethanol for several times to obtain CdS-L.

2.2. Preparation of CoS₂

2 mmol cobalt nitrate hexahydrate, 1 mmol ammonium fluoride and 5 mmol urea were added to 35 mL deionized water, stirred for 30 min, and reacted at 120 °C for 5 h. The hydrothermal product was washed twice with deionized water and absolute ethanol, respectively, and dried in an oven at 60 °C for 10 h. The obtained pink powder was calcined for 2 h at 400 °C, where it was the cobalt oxide precursor. A certain amount of cobalt oxide precursor and thioacetamide (mass ratio 1:3) were added to 50 mL deionized water, stirred for 20 min, and reacted at 180 °C for 20 h. The dry product after washing with deionized water and ethanol is CoS₂.

2.3. Preparation of CoS₂/CdS

A certain amount of CoS₂ and CdS-L were weighed and added into 20 mL ethanol, and the mixture was stirred by ultrasound for 1 h. The mixture solution was stirred continuously at 85 °C until dry. The resulting composite catalyst was named xCC-L (x represents the mass fraction of CoS₂ in CdS). xCC-R and xCC-P were prepared by the same method.

2.4. Characterization

The X-ray diffraction (XRD: SmartlabSE, Rigaku Corporation, Japan) was used to study the crystalline phase structure of catalysts. The microstructure and selected electron diffraction images of the catalyst were obtained by transmission electron microscope (TEM: JEM-2100, Rigaku Corporation, Japan). X-ray photoelectron spectroscopy (XPS: ESCALAB Xi+, Thermo Fisher Scientific, America) was used to study the elemental composition and valence distribution of the catalyst and the ultraviolet photoelectron spectroscopy (UPS) of the catalyst was measured by He I light source. The electron transfer of the catalyst was analyzed by XPS under in-situ illumination. The light absorption capacity of the catalyst was evaluated by UV-visible diffuse reflection spectrum (UV-2550, Shimadzu, Japan), and baseline calibration was performed using BaSO₄ powder. The photochemical properties of the catalyst were studied on a VersaStat 4-400 electrochemical workstation. The carrier kinetics of the catalyst was studied by fluorescence spectrometer (Fluoro Max-4, HoribaJobinYvon, America). The hydrogen evolution performance of the photocatalyst was evaluated using a multichannel photocatalytic reaction system (PCX50A Discover, Perfectlight, Beijing). The hydrogen evolution amount in the photocatalytic experiment was analyzed by gas chromatograph (GC7900, Techcomp) with nitrogen as carrier gas.

2.5. Photocatalytic hydrogen evolution experiment

First, 10 mg catalyst under test was added to a 60 mL glass bottle containing 30 mL 10 % lactic acid solution. After ultrasonic and stirring, the mixture was thoroughly mixed and the oxygen in the bottle and solution was replaced with nitrogen. Then, the bottle was put into a multi-channel photocatalytic reaction system with 5 W white light for hydrogen evolution for 5 h. 0.5 mL gas was extracted from the bottle and injected into the gas chromatograph every 1 h for analysis. The apparent quantum yield (AQY) is expressed as follows [26,27]:

$$AQY = \frac{N_e}{N_p} \times 100\% = \frac{1.2 \times 10^8 (vK)}{I \times A \times \lambda} \times 100\%$$

where, N_e is the total number of electrons transferred by reaction, N_p is the number of incident photons, v is the reaction rate, K is the number of electrons transferred by reaction, I is the optical power density, A is the area of incident light, and λ is the wavelength of incident light.

2.6. Computational details

All the density-functional theory (DFT) computations were performed using the pseudopotential plane wave method based on first-principles. Sections were performed on supercells of CdS $4 \times 2 \times 2$ and CoS₂ $2 \times 1 \times 1$. To avoid inter-layer interactions, a vacuum layer of 15 Å is used in the Z-direction. Electron-ion interactions were described using the ultrasoft potentials. For electron exchange and correlation interactions, the general gradient approximation (GGA) of Perdew-Burke-Ernzerhof (PBE) functional parameters is used. The k-points used the Monkhorst-Pack grid with the separation set to 0.06 \AA^{-1} . For the hydrogen adsorption model, the PWC functional of the local density

approximation (LDA) method was used to optimize the structure and calculate the frequency. The custom grid parameter for k-points is $3 \times 3 \times 1$. The Gibbs free energy is calculated by the following equation [28]:

$$\Delta G_{H^*} = \Delta E_{H^*} + \Delta E_{ZPE} - T\Delta S.$$

where ΔE_{ZPE} and $T\Delta S$ are the zero-point energy and entropy change of H₂ and adsorption phase respectively. The energy of ΔE_{H^*} is calculated as follows:

$$\Delta E_{H^*} = E_{H^*} - E - 1/2E_{H_2}.$$

where E and E_{H_2} are the total energy of the substrate and hydrogen, and E_{H^*} is the total energy of the substrate adsorbing hydrogen.

The d-band center is calculated as follows:

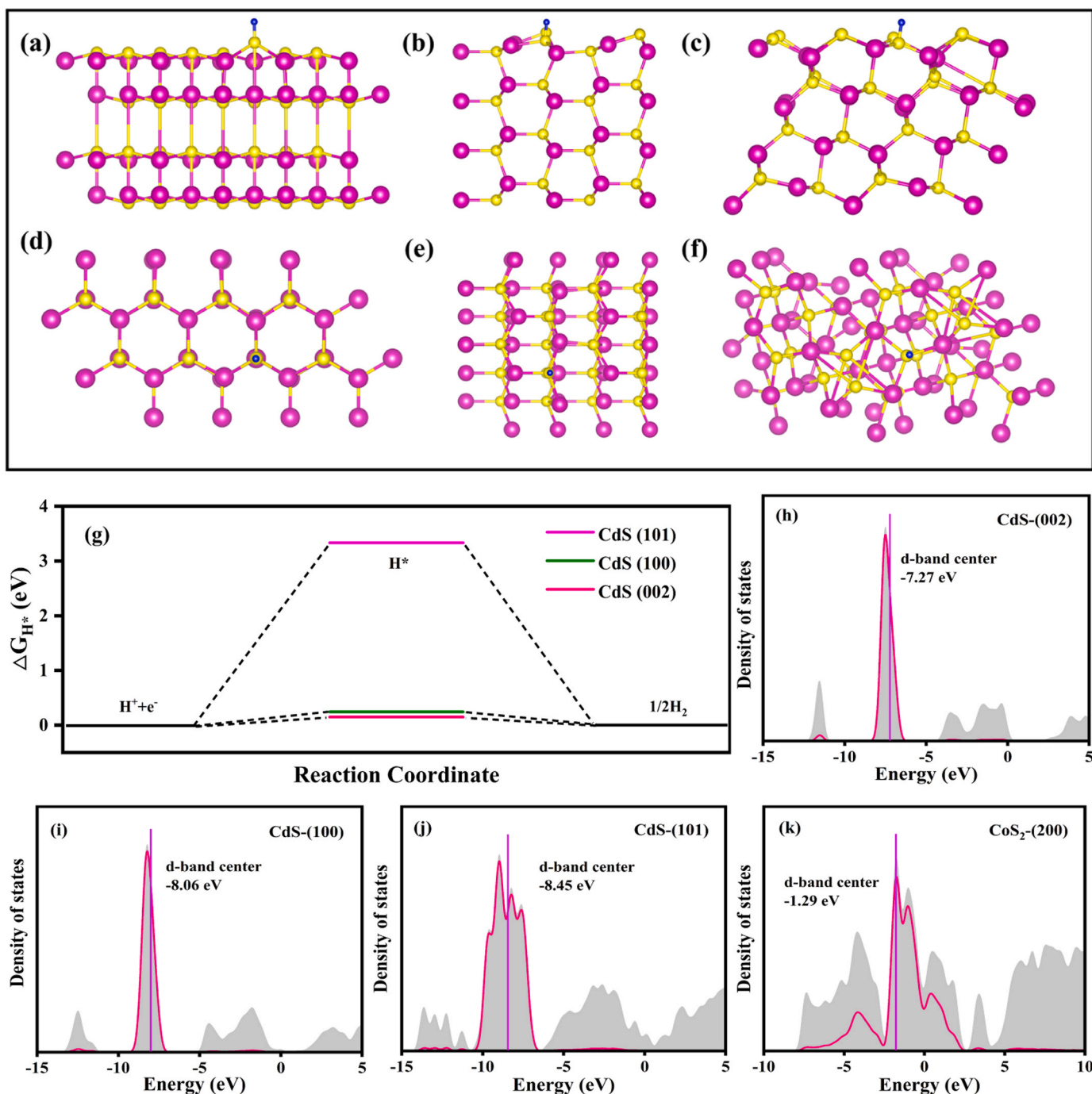


Fig. 1. Side view of hydrogen adsorption model of CdS (002) (a), CdS (100) (b) and CdS (101) (c); Top view of hydrogen adsorption model of CdS (002) (d), CdS (100) (e) and CdS (101) (f); Red represents the Cd atom, yellow represents the S atom, and blue represents the H atom; Gibbs free energy of hydrogen adsorption on different crystal faces of CdS (g); the d-band center of CdS (002) (h), CdS (100) (i), CdS (101) (j) and CoS₂ (200) (k).

$$\varepsilon_d = \frac{\int_{-\infty}^{\infty} n_d(\varepsilon) \varepsilon d\varepsilon}{\int_{-\infty}^{\infty} n_d(\varepsilon) d\varepsilon}$$

where, ε is the energy level, $n_d(\varepsilon)$ is the density of states. The calculation data of the D-band center are in Table S1.

3. Results and discussion

3.1. DFT analysis

The density functional theory (DFT) based on first principles is used

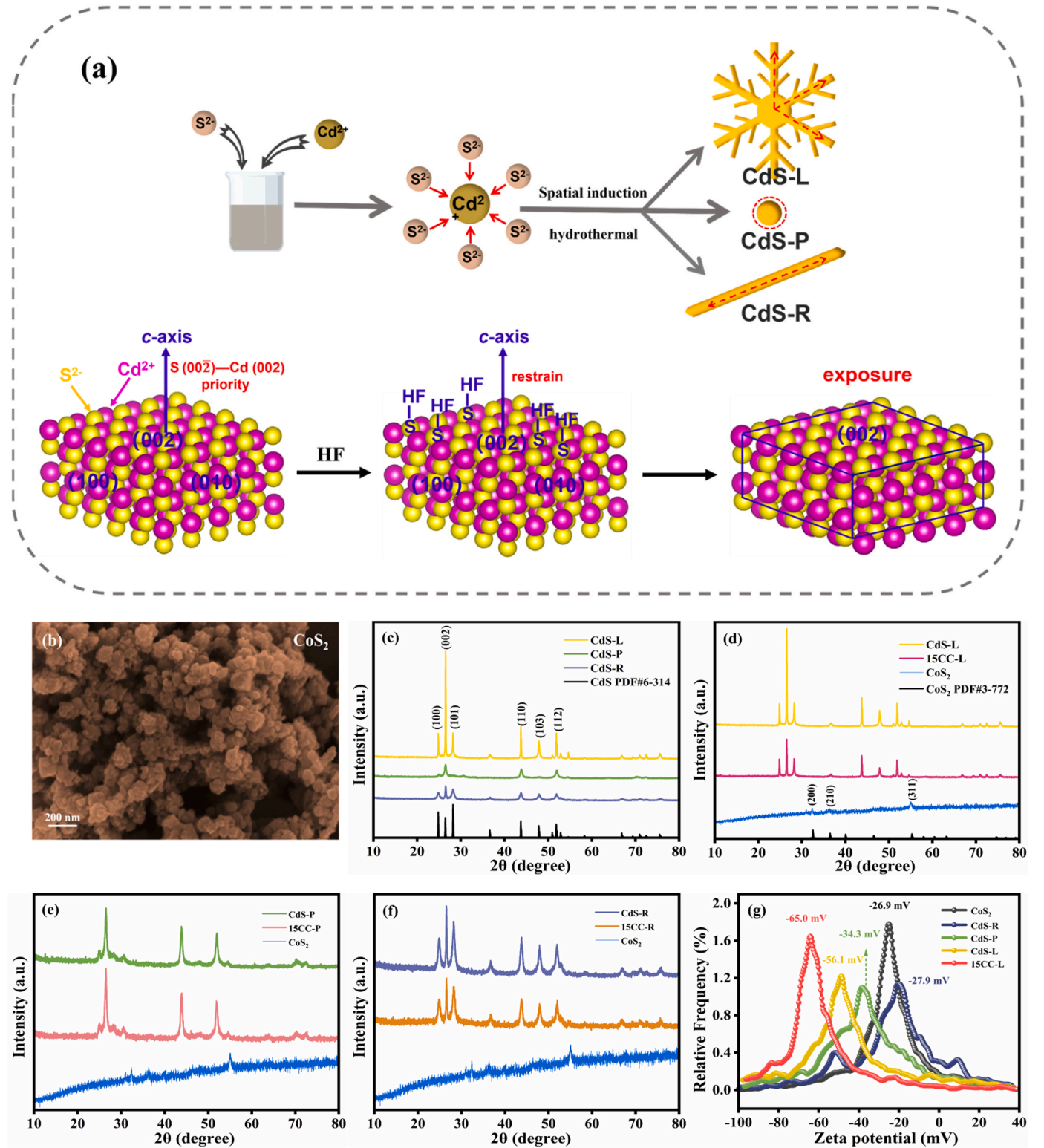


Fig. 2. Preparation diagram of CdS with different morphologies (a); SEM image of CoS₂ nanoparticles (b); XRD patterns of CdS-R, CdS-P and CdS-L (c); XRD patterns of CdS-L, CoS₂ and 15CC-L (d); XRD patterns of CdS-P and 15CC-P (e); XRD patterns of CdS-R and 15CC-R (f); Zeta potentials of CoS₂, CdS-R, CdS-P, CdS-L and 15CC-L (g).

to analyze CdS with different crystal orientations, and the potential differences in properties are discussed, which provides theoretical guidance for experiments. The interfacial properties resulting from different exposures of crystal planes vary greatly, and the hydrogen adsorption Gibbs free energy (ΔG_{H^*}) is an important theoretical indicator to evaluate the hydrogen production performance of the catalyst [29]. As shown in Fig. 1a-f, the structure optimization of hydrogen adsorption models on several CdS surfaces was carried out. Fig. 1a-c depict the top view of hydrogen adsorption models on CdS (002), CdS (100) and CdS (101), respectively, while Fig. 1d-f shows their side views. The more positive the ΔG_{H^*} , the less favorable the occurrence of the Volmer reaction, and the more negative the ΔG_{H^*} , the less favorable the occurrence of the Heyrovsky and Tafel reactions. Therefore, the more the ΔG_{H^*} is close to zero, the higher the hydrogen production activity of the catalyst [30]. According to Fig. 1g, the ΔG_{H^*} values for CdS (002), CdS (100) and CdS (101) are 0.21 eV, 0.24 eV and 3.33 eV, respectively. The (002) crystal plane is a highly active in hydrogen production for CdS, whereas the (101) crystal plane does not significantly contribute to the hydrogen evolution reaction. The work function (ϕ) is also an important surface property of semiconductors. The theory of π -band center is an important theoretical property for evaluating the catalytic activity of transition metal catalysts. The π -band of the transition metal couples with the adsorbate leading to the formation of an antibonding energy band. The closer the π -band center is to the Fermi level, the less filled the antibonding energy level becomes with electrons, resulting in stronger bonding stability and adsorption strength. As shown in Fig. 1h-k, the π -band center (-7.27 eV) of CdS (002) is closer to the Fermi level, indicating that the (002) crystal plane is the best catalytically active crystal plane. Furthermore, the π -band center (-1.29 eV) of CoS₂ (200) is further elevated, and the equilibrium between adsorption and desorption enables it to function as an effective co-catalyst for enhancing the rate of photocatalytic hydrogen evolution reaction in the composite system. In summary, theoretical calculations have determined that CdS (002) is a highly reactive hydrogen evolution crystalline surface, providing a theoretical basis for subsequent experiments.

3.2. Structure and morphology

The crystal structure of the catalyst was analyzed by X-ray diffraction (XRD). By changing the sulfur source and solvent, the growth of CdS structure cells in different spatial dimensions is realized to induce the ideal crystal surface exposure (Fig. 2a). During the crystal growth process in which Cd²⁺ ions and S²⁻ ions are coordinated, positively charged Cd (002) planes and negatively charged S (00 $\bar{2}$) planes are alternately stacked and grown along the polar axis c -axis, so the growth rate and priority of (002) planes over other surfaces due to higher atomic density and metastability. The small facets appear or even disappear under the rapid growth of the crystal, so the strong hydrogen bond acceptor HF molecules are introduced to combine with the S atoms on the (002) face to form S-HF. The presence of HF molecules inhibits the asymmetric growth of the (002) crystal plane of CdS on the c -axis resulting in the exposure of the (002) crystal plane. A group of crystal planes in the direction perpendicular to the c -axis grow synchronously in six directions to form uniform six branches due to its hexagonal unit cell. Fig. 2b shows CoS₂ as a tiny nanoparticle structure, which has undergone agglomeration due to the absence of a well-dispersed carrier. As shown in Fig. 2c, all three CdS samples correspond to the hexagonal phase (PDF#6-314), but their crystal forms differ significantly due to distinct growth mechanisms. Unlike the typical mixed crystal plane of CdS-R, CdS-L and CdS-P exhibit a strong preference for the growth of (002). CdS-P has extremely weak (100) and (101) crystal faces, while (002) crystal faces are well exposed but relatively weak crystallinity. Although there are other crystal faces of CdS-L, the (002) crystal face exhibits the highest relative strength, and its activity may be affected by the degree of exposure and crystallinity. Fig. 2d-f show the XRD patterns

of different composite catalysts. The corresponding CdS characteristic peak can be observed obviously in the composite catalyst, while the CoS₂ characteristic peak is not visible due to its small size and low content. As shown in Fig. 2g, the Zeta potential of the catalyst was tested by electrophoresis. All catalysts exhibit a negative surface potential, which provides a favorable environment for ion adsorption. The surface potential of cadmium sulfide becomes increasingly negative as the exposure of (002) crystal plane increases, indicating that (002) crystal plane is an effective active site. In addition, the Zeta potential of the composite catalyst reached -65.0 mV, proving that it is a stable architecture.

The microstructure and crystal characteristics of the catalyst were studied by transmission electron microscopy (TEM). Fig. 3a-b are the microscopic morphologies of rod-like and particle CdS, both of which exhibit nanometer dimensions. Fig. 3c and Fig. 3d are high-resolution transmission electron microscope (HRTEM) images of CdS-R and CdS-P, respectively. In order to better study their crystal plane distribution, their high-resolution lattice fringe images were obtained by Fast Fourier Transform (FFT) (Fig. 3g-h). For CdS-R, the two ends are more (002) crystal planes, and the middle part is the exposed area of (100) crystal planes. The rod-like structure formed along the (002) crystal plane may be more conducive to space charge separation and material transfer, which is one of the reasons for the high activity of CdS-R in previous studies. As shown in Fig. 3h, different regions of CdS-P display different crystal planes (002 crystal plane or 100 crystal plane), and it has no specific morphology, which means that its crystal growth has no specific rules, which is not conducive to high activity exposure of crystal faces. Fig. 3e and Fig. 3f are selected electron diffraction (SAED) images of CdS-R and CdS-P, respectively. According to the images, they all belong to polycrystals, and the corresponding crystal planes have strong diffraction rings, showing the characteristics of mixed coexistence of multiple crystal planes.

As shown in Fig. 4a-b, CdS-L presents a "leaf-like" microscopic morphology that extends synchronously in six directions. Fig. S1 shows the SEM image of CdS-L, which displays a "leaf-like" CdS structure with uniform growth in six directions. In order to explore its crystal plane orientation, HRTEM and SAED images of its different regions were obtained. The HRTEM images of different regions of CdS-L were selected for analysis, as shown in Fig. 4f-h, corresponding to Region 1, Region 2 and Region 3 in Fig. 4b, respectively. Fig. 4i-k clearly shows that there are lattice fringes corresponding to CdS (002) in all three regions, which is related to the exposure degree of the high (002) crystal plane. Fig. 4c-e are the SAED images of the top, bottom and leaves of CdS-L, respectively, and their diffraction regions are marked in Fig. 4b. It can be seen that there are more diffractions belonging to the (110) crystal plane and (100) crystal plane at the top and bottom, while the blades show strong diffraction of the (002) crystal plane and (110) crystal plane. From the above results, it can be seen that the hexagonal unit cell of CdS-L grows along the (110), (100) crystal planes and a group of their equivalent crystal planes to form branches extending synchronously in six directions, and the (002) crystal plane direction asymmetric growth was inhibited, and a large number of (002) crystal planes were exposed on the flat leaves surface. Furthermore, unlike the polycrystalline nature of CdS-R and CdS-P, CdS-L exhibits distinct monocrystal features. The atoms inside the single crystal are regularly and periodically arranged in three-dimensional space, and its anisotropic environment also provides additional selectivity for the reaction to occur. Single-crystal catalysts are usually easier to achieve the effect of exposed crystal faces, have stronger charge transport ability and chemical stability, and help to achieve stronger photocatalytic performance.

Fig. 4l is the TEM image of 15CC-L, from which it can be observed that CoS₂ particles are loaded on the leaves of CdS-L. Due to the three-dimensional nature of the spatial structure, Fig. 4m and Fig. 4n are the lattice fringe images of the CdS-L and CoS₂ interfaces at different focusing degrees. It can be observed that the lattice spacing at $d = 0.28$ nm and $d = 0.33$ nm corresponds to the CoS₂ (200) crystal plane

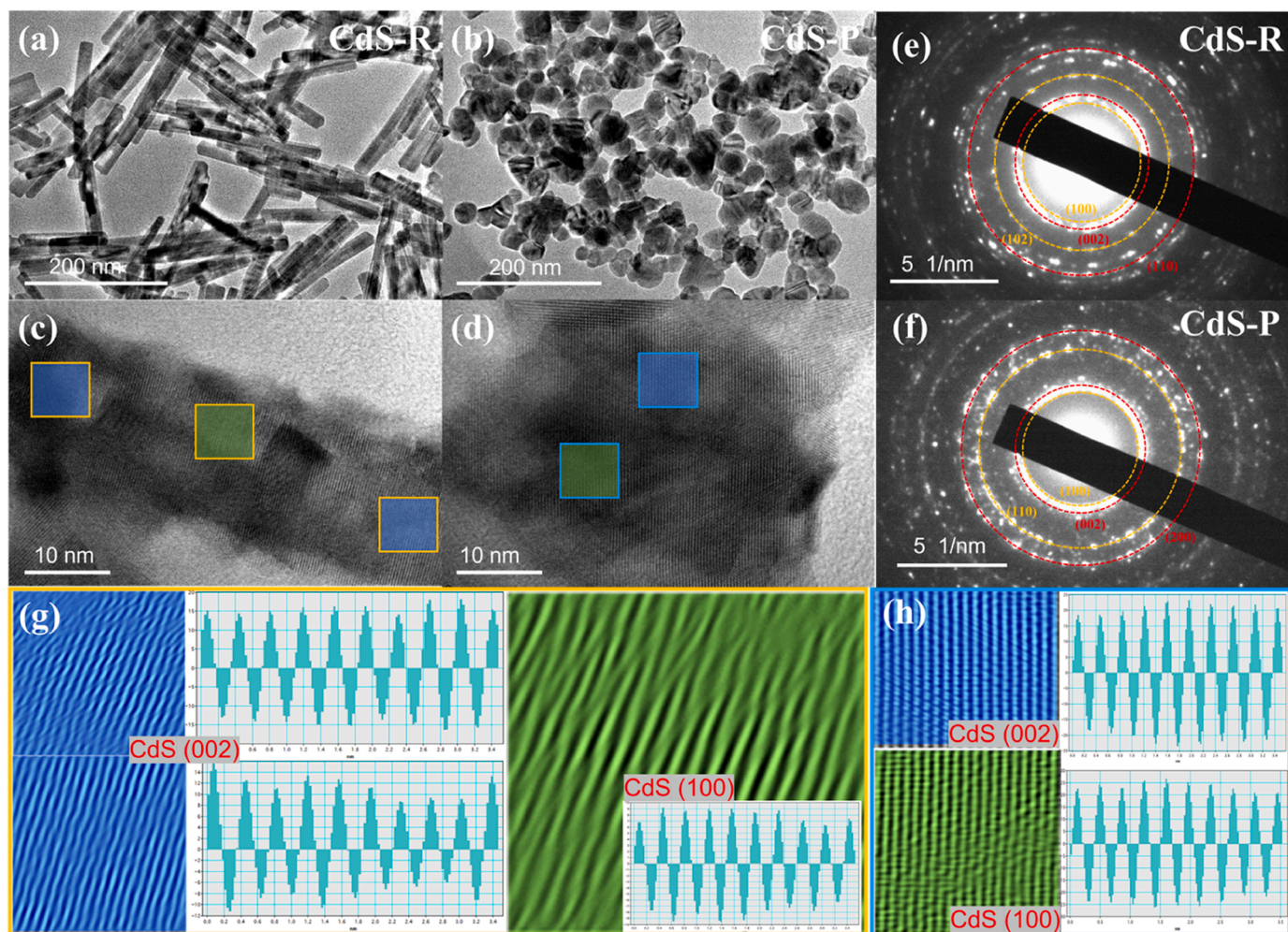


Fig. 3. TEM and HRTEM images of CdS-R (a, c), CdS-P (b, d); SAED images of CdS-R (e), CdS-P (f); lattice fringe images of CdS-R (g) and CdS-P (h) using Fast Fourier Transform (FFT).

and the CdS (002) crystal plane, respectively.

The elemental composition and valence distribution of the catalyst surface were investigated by X-ray photoelectron spectroscopy (XPS). The XPS full spectrum in Fig. 5a displays the elemental composition of each catalyst and confirms the absence of impurities. Fig. 5b shows the XPS fine spectrum of Cd 3d. The peaks at 411.52 eV and 404.73 eV are Cd 3d_{3/2} and Cd 3d_{5/2}, respectively, where Cd is present in the +2 valence state [31,32]. Fig. 5c shows the XPS fine spectrum of Co 3d with peaks at 794.36 eV and 779.20 eV attributed to Co³⁺ 3d_{3/2} and Co³⁺ 3d_{5/2}, while the peaks at 798.93 eV and 782.03 eV belong to Co²⁺ 3d_{3/2} and Co²⁺ 3d_{5/2}, respectively [33]. The element Co is present in the mixed valence form, so a clear satellite peak appears. As shown in Fig. 5d, S 2p in CdS-L split into two peaks at 162.30 eV and 161.08 eV, attributed to S 2p_{1/2} and S 2p_{3/2}, respectively [34]. CoS₂ and 15CC-L also exhibit the peaks of S²⁻ at corresponding binding energy positions [35,36]. The difference is that CoS₂ shows the distinct S-O binding energy peak at 169.10 eV and 167.97 eV in addition to the S-Co binding energy peak at 162 eV because of the surface oxidation. Fig. 5e-f shows the Cd 3d fine spectrum and S 2p fine spectrum of different CdS, and it can be seen that their elemental compositions and valence states are consistent. In addition, the binding energy of the elements in the composite catalyst is slightly shifted, indicating the interaction between CdS and CoS₂ [37].

3.3. Hydrogen evolution kinetics analysis

The differences in the electronic structure of catalysts will result in different optical properties. The light absorption capacity and bandgap of the catalyst were studied by UV-visible diffuse reflectance spectroscopy (UV-vis DRS). As shown in Fig. 6a, CdS-R and CdS-L have similar absorption spectra, and their absorption band edges are around 550 nm. The CdS-P has a wider range of light absorption, but its light absorption ability is weakened. It is obvious that CoS₂ has a strong light absorption capacity in the whole spectral region, and the light absorption capacity of the loaded composite catalyst is greatly improved compared with that of single CdS. The bandgap of the semiconductor can be obtained by Tauc Plot method. Fig. 6b shows the bandgap diagrams of CdS with different crystal faces obtained by using the formula (1) [38]. The bandgaps of CdS-R, CdS-P and CdS-L are 2.36 eV, 2.35 eV and 2.15 eV, respectively. From the above analysis, it can be seen that the light absorption capacity and bandgap of the three CdS are different to some extent, but this may not be the main reason affecting their photocatalytic activity.

$$(ah\nu)^{1/n} = A(h\nu - E_g) \quad (1)$$

α is the light absorption index; h denotes the Planck constant; ν denotes the frequency; E_g is the semiconductor band gap; direct bandgap semiconductor $n = 1/2$, indirect bandgap semiconductor $n = 2$.

The catalyst intrinsic carrier transfer mechanism was investigated by photoluminescence (PL) spectroscopy. As shown in Fig. 6c, the peak

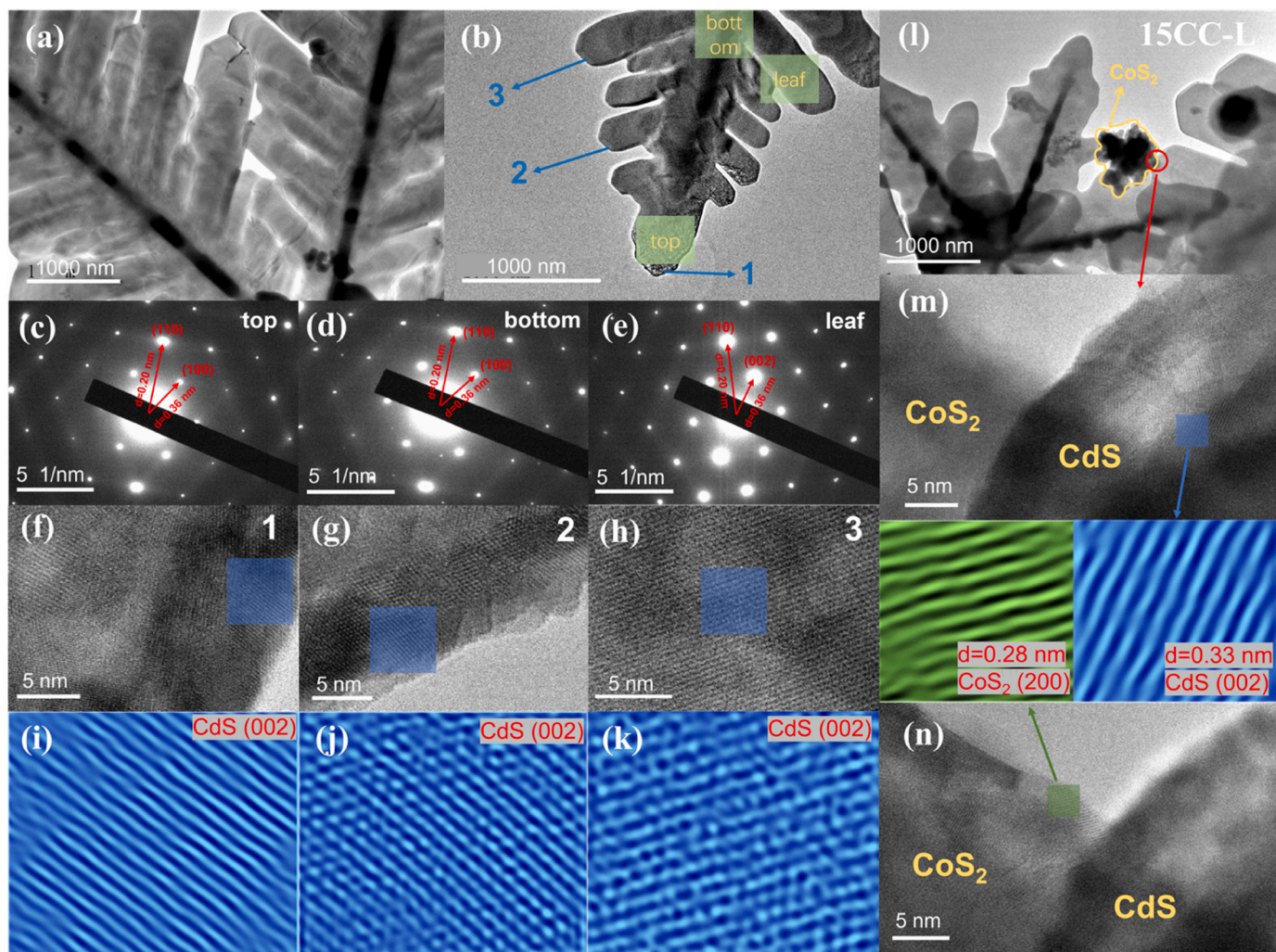


Fig. 4. TEM images of CdS-L (a, b) and 15CC-L (l); SAED images of CdS-L (c, d, e) and 15CC-L (m, n); lattice fringe images of CdS-L (f, g, h); lattice fringe images of CdS-L using FFT (i, j, k).

intensity of steady-state fluorescence represents the energy released by the process of returning the excited molecule to the ground state. At the excitation wavelength of 380 nm, the three CdS showed emission peaks at longer wavelengths due to the Stokes shift effect. It is worth noting that the maximum emission peaks of CdS-R, CdS-P, CdS-L show a red shift phenomenon, which is caused by less energy loss. CdS-L has the largest fluorescence emission wavelength, which represents less energy loss during its vibrational relaxation and fluorescence emission. Therefore, we can infer that the exposure of the (002) crystal plane makes the CdS molecule more in the excited state upon excitation, which facilitates the participation in the photocatalytic reaction process. In addition, the fluorescence emission intensity of the composite catalysts are all smaller than that of pure CdS, which indicates that the complexation rate of photogenerated electrons and holes is effectively suppressed. The time-resolved photoluminescence (TRPL) spectroscopy were studied to obtain the fluorescence lifetimes of the catalysts. The time-resolved photoluminescence spectra shown in Fig. 6d were obtained by multi-exponential fitting of function (2) [39], and the fluorescence lifetimes and their related parameters in Table 1 were obtained using function (3) [40].

$$I(t) = \sum_{i=1,2,3} B_i e^{-t/\tau_i} \quad (2)$$

I is the normalized emission intensity; t is the time after the pulsed laser excitation; τ_i are the respective decay lifetimes; B_i are the

corresponding weight factors.

$$\langle \tau \rangle = \frac{\sum_{i=1,2,3} B_i \tau_i^2}{\sum_{i=1,2,3} B_i \tau_i} \quad (3)$$

$\langle \tau \rangle$ is the average lifetime; τ_i are the respective decay times; B_i are the corresponding weight factors.

The fluorescence lifetimes of CdS-R, CdS-P, CdS-L gradually increase, and the longer fluorescence lifetimes in a single catalyst represent the ability of the photogenerated electrons to participate in the photocatalytic reaction for a longer period of time. The exposure of highly reactive (002) crystalline face induces more charges to participate in the surface reaction, which is manifested as an increase in fluorescence lifetime. The difference is that the fluorescence lifetimes of the composite catalysts are all smaller than those of the single catalysts due to the fluorescence quenching effect generated by the rapid electron transfer between the catalyst interfaces. [Fig. S2](#) and [Table S2](#) display the fluorescence lifetime data for various proportions of xCC-L, revealing that higher photocatalytic hydrogen evolution activity is associated with a shorter fluorescence lifetime.

The intrinsic charge mechanism of catalysts can be explored by photoelectric chemistry experiment. Fig. 7a shows the transient photocurrent response curves of the catalyst under intermittent light illumination. CoS₂ has almost no photocurrent response, and the metalloid and electron collector properties dictate that it cannot generate

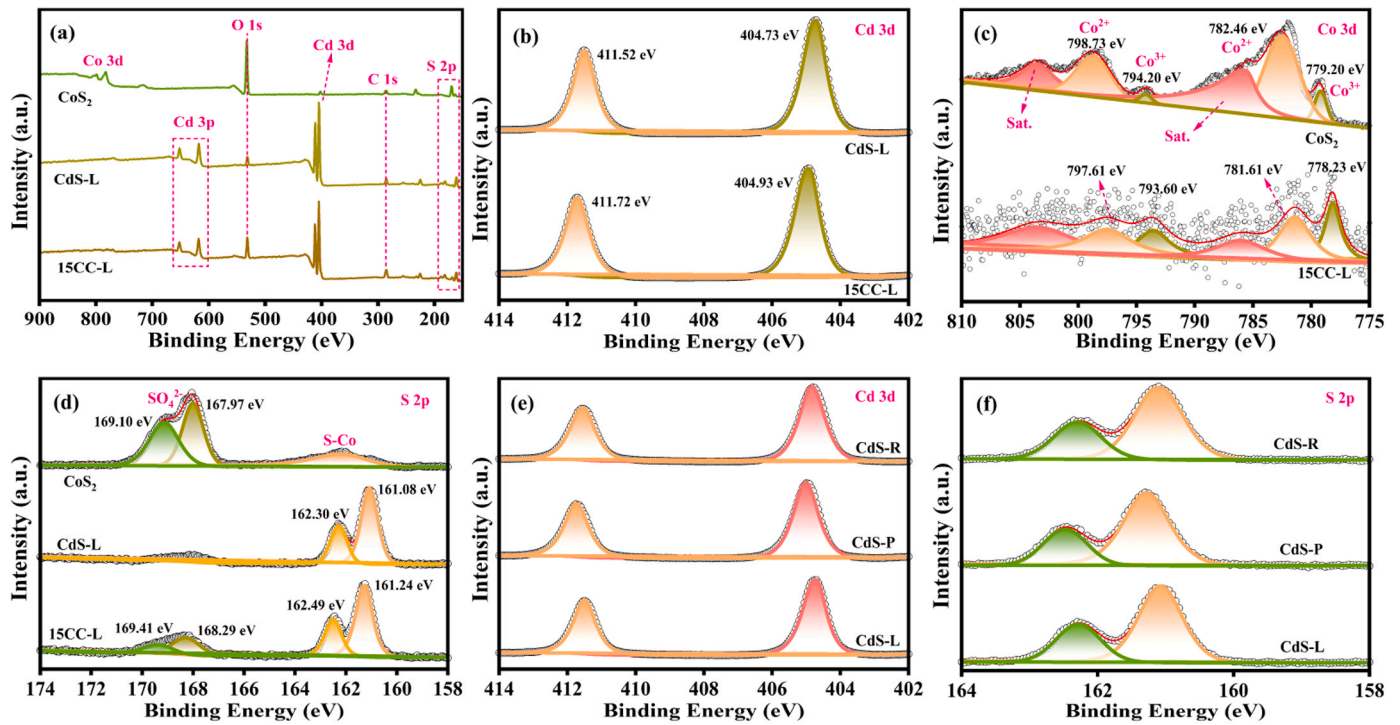


Fig. 5. XPS full spectra of CoS₂, CdS-L and 15CC-L (a); Cd 3d fine spectrum of CdS-L and 15CC-L (b); Co 3d fine spectrum of CoS₂ and 15CC-L (c); S 2p fine spectrum of CdS-L and 15CC-L (d); Cd 3d fine spectrum of CdS-R, CdS-P and CdS-L (e); S 2p fine spectrum of CdS-R, CdS-P and CdS-L (f).

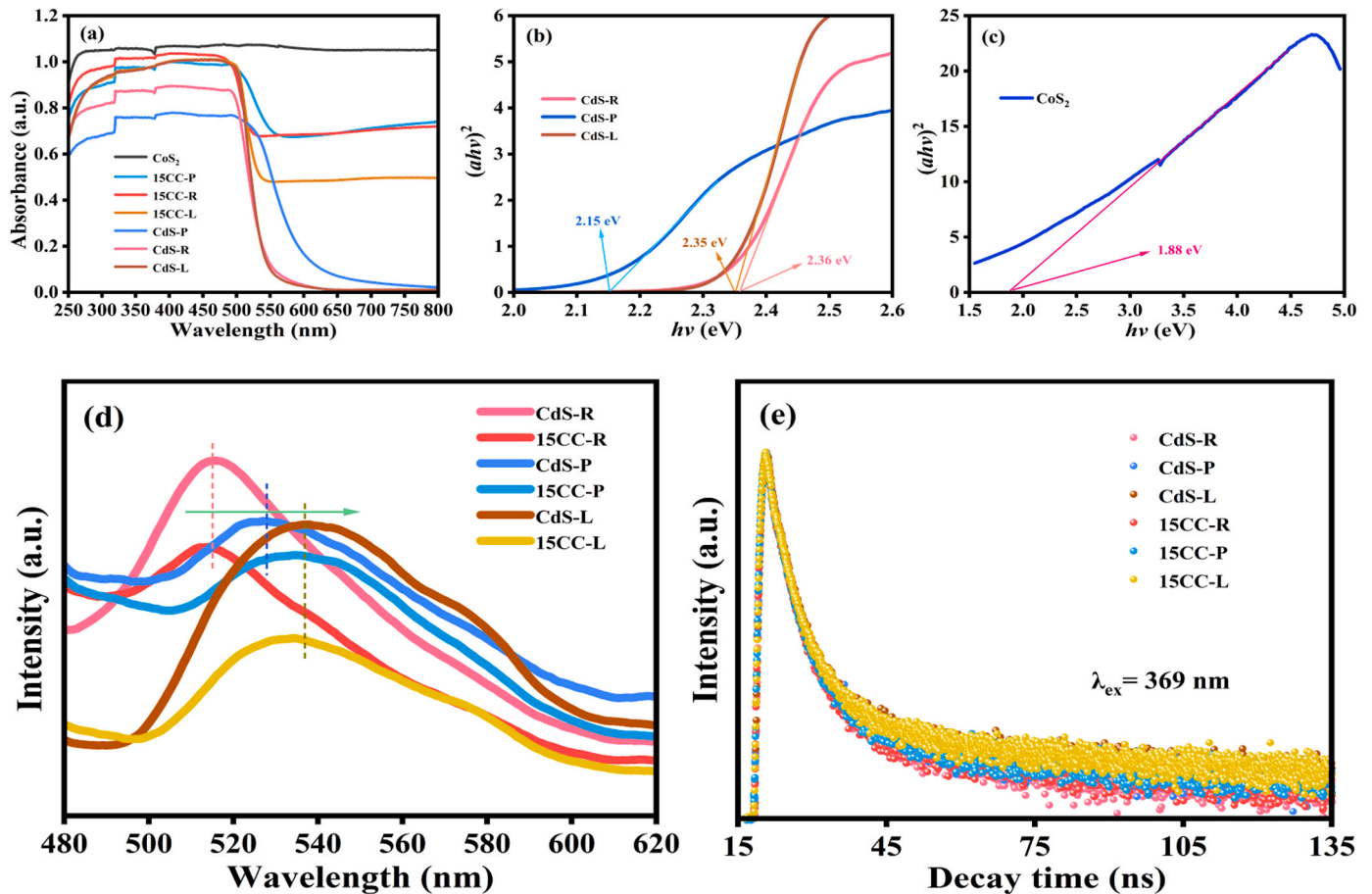


Fig. 6. UV-vis DRS patterns of all catalysts (a); the bandgaps of CdS-x (x = R, P, L) (b) and CoS₂ (c); steady-state fluorescence response of all catalysts (d); time resolved photoluminescence spectrum of all catalysts (e).

Table 1

The exponential curve fitted parameters of emission decay for catalysts.

Sample	Lifetime, τ (ns)	Rel (%)	$\langle \tau \rangle$ (ns)	χ^2
CdS-R	$\tau_1 = 0.86$	$A_1 = 44.27$	1.73	1.54
	$\tau_2 = 4.67$	$A_2 = 29.62$		
	$\tau_3 = 143$	$A_3 = 26.11$		
CdS-P	$\tau_1 = 4.78$	$A_1 = 29.52$	1.83	1.59
	$\tau_2 = 142$	$A_2 = 27.70$		
	$\tau_3 = 0.88$	$A_3 = 42.78$		
CdS-L	$\tau_1 = 4.78$	$A_1 = 28.45$	2.03	1.47
	$\tau_2 = 0.92$	$A_2 = 39.67$		
	$\tau_3 = 151$	$A_3 = 31.88$		
15CC-R	$\tau_1 = 4.63$	$A_1 = 29.46$	1.68	1.49
	$\tau_2 = 144$	$A_2 = 26.79$		
	$\tau_3 = 0.82$	$A_3 = 43.75$		
15CC-P	$\tau_1 = 4.65$	$A_1 = 29.59$	1.75	1.49
	$\tau_2 = 141$	$A_2 = 27.57$		
	$\tau_3 = 0.84$	$A_3 = 42.84$		
15CC-L	$\tau_1 = 4.42$	$A_1 = 29.41$	1.92	1.49
	$\tau_2 = 142$	$A_2 = 31.20$		
	$\tau_3 = 0.87$	$A_3 = 39.39$		

photogenerated charges. Corresponding to the hydrogen producing activity of CdS with different degrees of crystal surface exposure, CdS-L has the strongest photocurrent response. When loaded with CoS₂, they showed a significant enhancement in the degree of photocurrent response, indicating that the separation efficiency of photogenerated carriers was significantly improved. Fig. 7b shows the linear scanning voltammetric (LSV) curves of each catalyst. The hydrogen evolution overpotential reflects the degree of polarization of the catalyst in the hydrogenolysis reaction, and the smaller its absolute value, the more favorable the H⁺ reduction reaction occurs. It is evident that the composite catalyst exhibits a smaller overpotential compared to the single catalyst, while the exposure of the stronger (002) crystal plane also lead to a reduced overpotential for the corresponding CdS. Electrochemical impedance spectroscopy (EIS) allows to study the intrinsic resistance of

catalysts and thus to understand the strengths and weaknesses of charge transfer performance. As shown in Fig. 7c, the magnitude of the radius of curvature reflects the magnitude of the catalyst resistance. CoS₂ has a very low charge resistance due to its metallic nature, and the interfacial charge transfer resistance of CdS-L is less than that of CdS-R and CdS-P. The ordered arrangement of crystalline grains within single crystal CdS-L provides a path for efficient charge transfer, which is an important reason for its increased electrical conductivity. At the same time, the introduction of CoS₂ effectively weakens the resistance of the catalyst and thus facilitates the interfacial transfer of electrons. Fig. 7d shows the Tafel curves of the catalysts under irradiation using a 300 W xenon lamp. It can be seen that the polarization overpotential of 15CC-R is smaller than that of CdS, compared to 15CC-L which has the smallest polarization overpotential. This difference represents a significant increase in reducing power, and CoS₂ can effectively induce charge transfer [41,42].

3.4. Photocatalytic hydrogen evolution activity

The activity of the catalysts was investigated by photocatalytic hydrogen production experiments. As shown in Fig. 8a, there is a significant increase in the hydrogen production activity of CdS with the increase of (002) crystal plane exposure. The hydrogen production activity of CdS-L is two times higher than that of CdS-R, which indicates that the (002) crystal plane is an efficient active site for photocatalytic hydrogen evolution. CoS₂ itself does not possess hydrogen production activity, but its loading onto CdS-L resulted in a hydrogen production amount of 961 μmol for 5 h. The hydrogen evolution activity of 15CC-R and 15CC-P is also significantly improved compared with that of single CdS. Fig. 8b shows the photocatalytic hydrogen evolution of CdS with different CoS₂ loads. Appropriate loads can give full play to the photocatalytic performance of CdS, while excessive loads will hinder the use of light by CdS, resulting in reduced hydrogen evolution activity. To demonstrate the stability and accuracy of the hydrogen production data,

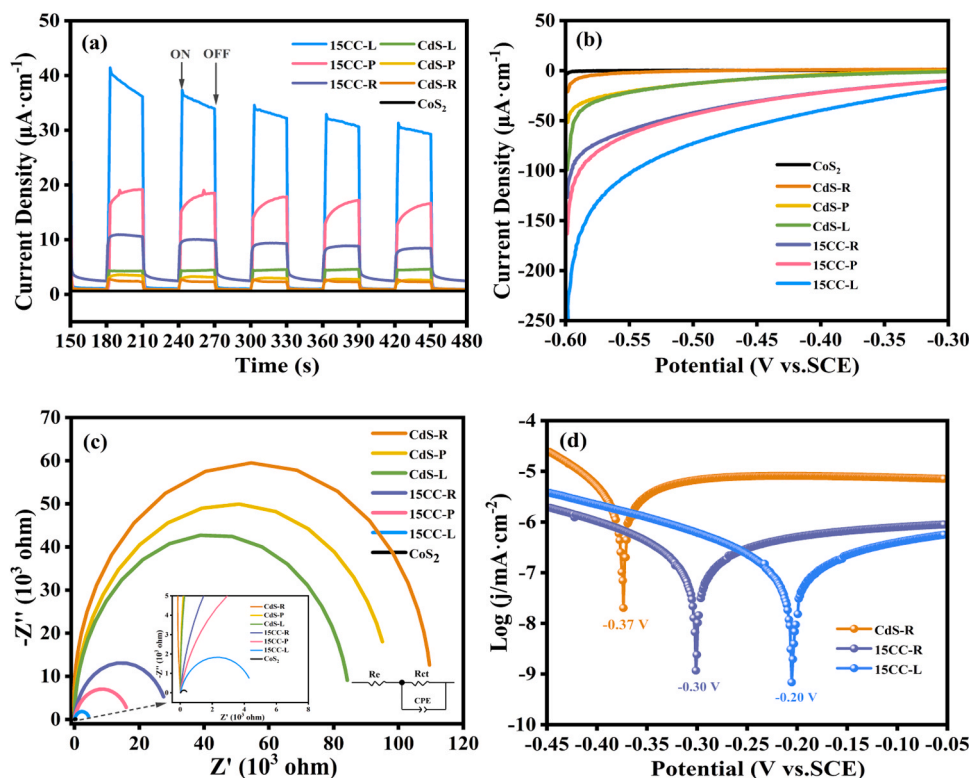


Fig. 7. Transient photocurrent response curve of each catalyst (a); linear sweep voltammetry curve of each catalyst (b); electrochemical impedance spectra of each catalyst (c); tafel curve of CdS-R, 15CC-R and 15CC-L under light (d).

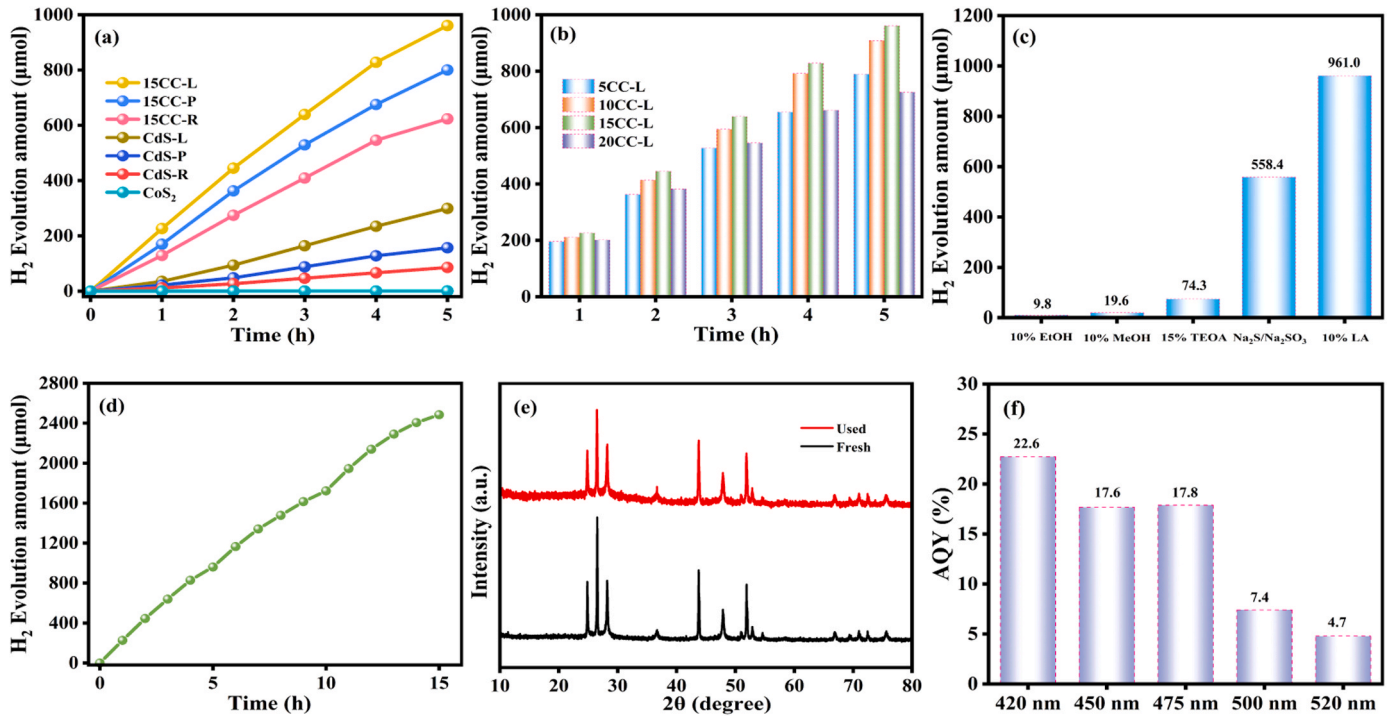


Fig. 8. Hydrogen evolution amount of each catalyst (a); hydrogen evolution of composite catalysts xCC-L ($x = 5, 10, 15, 20$) (b); hydrogen evolution amount of 15CC-L with different sacrificial reagents (c); hydrogen evolution activity of 15 CC-L for 15 h (d); XRD pattern of 15CC-L before and after hydrogen production (e); the AQY of 15CC-L under different wavelength light sources (f).

Fig. S3 presents the photocatalytic hydrogen evolution data with error bars. To investigate the optimal environment for hydrogen production, the experiment was conducted as shown in Fig. 8c. The composite catalyst can achieve high hydrogen evolution activity in the system with 10 % LA and Na₂S/Na₂SO₃ (0.35 M/0.25 M) as sacrificial reagents, while the other sacrificial reagents only show very weak activity. Stability is one of the important indexes to evaluate the performance of photocatalyst. As shown in Fig. 8d, continuous hydrogen evolution experiments were carried out for 15 h on composite catalyst 15CC-L, and it can be seen that its hydrogen evolution quantity maintained linear growth. The XRD spectra before and after hydrogen production characterized the structural stability of the catalyst. As shown in Fig. 8e, the XRD spectra of the composite catalyst after hydrogen production showed no excess diffraction peaks, indicating its good stability. The apparent quantum yield is an important index to evaluate the utilization of light energy by photocatalysts. As shown in Fig. 8f, the apparent quantum yield of 15CC-L was tested at different cutoff wavelengths. It has a good light energy utilization efficiency from 420 to 475 nm, and the highest apparent quantum yield (AQY) at 420 nm reaches 22.6 %. The hydrogen production activity of CdS-L and 15CC-L is compared with

other CdS-based photocatalysts reported in the literature, as shown in Table S3. The hydrogen evolution activity of both single CdS-L and composite catalyst 15CC-L is higher than that of other reported catalysts, which reflects the advantages of the CdS-L with (002) crystal face exposure for photocatalytic hydrogen evolution.

The difference in specific surface area accompanying different morphologies is also an important factor affecting the catalyst activity. The specific surface area and pore size distribution of catalysts were tested by Brunauer Emmett Tellerf (BET) method. The N₂ adsorption and desorption curves and pore size distribution curves of the three forms of CdS are shown in Fig. 9a-c and Table 2. From the adsorption isotherms

Table 2

The S_{BET}, pore volume and average pore size of CdS-R, CdS-P, CdS-L.

Samples	S _{BET} / (m ² /g)	Pore volume / (cm ³ /g)	Average pore size / nm
CdS-R	53.21	0.27	18.21
CdS-P	36.34	0.34	34.33
CdS-L	9.90	0.02	7.53

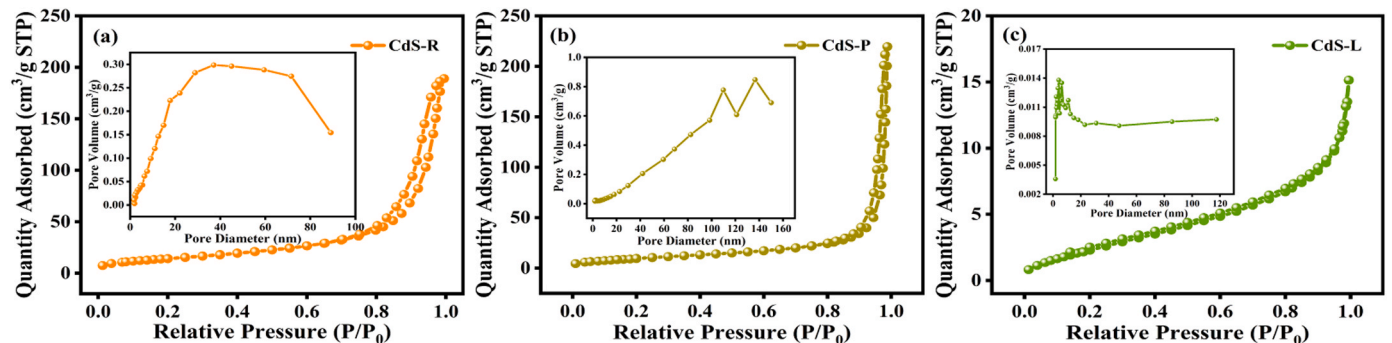


Fig. 9. Nitrogen adsorption desorption curves and pore size distribution curves of CdS-R, CdS-P and CdS-L.

and pore size distribution intervals, it is known that they are all mesoporous materials. It should be noted that CdS-L has the best hydrogen evolution activity, but its specific surface area and pore size are the smallest. The above phenomena suggest that morphology and specific surface area are not the main factors to enhance the photocatalytic activity of CdS-L, but rather because of its more highly active (002)

crystalline surface. Meanwhile, single crystal CdS-L possesses higher chemical stability and inherent periodic pore channels, which provide anisotropic sites for catalytic reactions to occur.

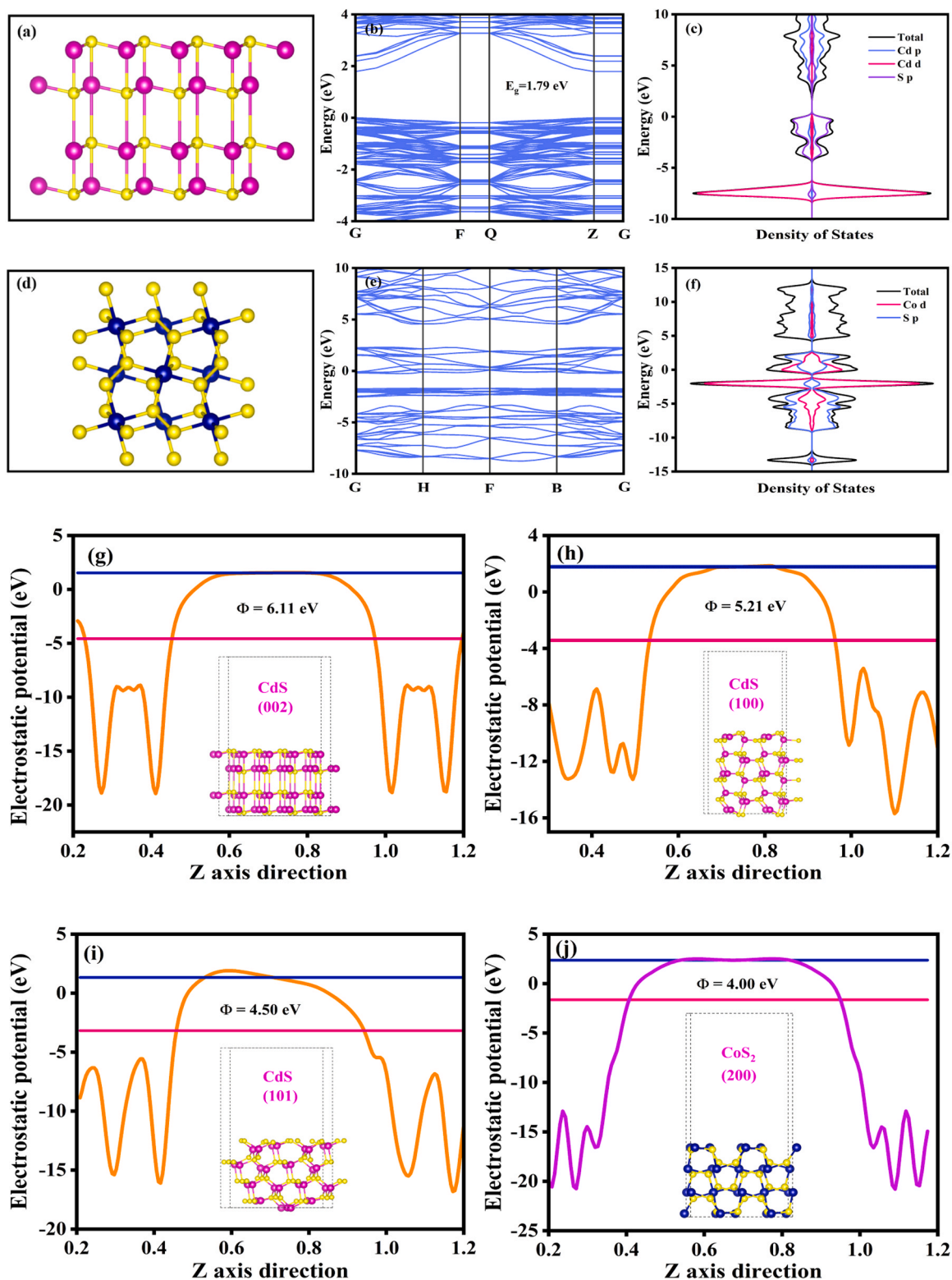


Fig. 10. The optimized structure of CdS (002) (a) and CoS₂ bulk (d); the band structure image of CdS (002) (b) and CoS₂ bulk (e); the partial density of states of CdS (002) (c) and CoS₂ bulk (f); the work function of CdS (002) (g), CdS (100) (h), CdS (101) (i) and CoS₂ (200) (j).

3.5. Electronic structure and surface properties

The electronic structures of CdS and CoS₂ are studied by density functional theory (DFT) based on first principles. The optimized structures of CdS (002) and CoS₂ are shown in Fig. 10a and Fig. 10d, respectively. Among them, the space group of hexagonal CdS is P63mc and the space group of cubic CoS₂ is Pa-3. As shown in Fig. 10b-c, CdS (002) is a direct bandgap semiconductor with a bandgap of 1.79 eV, and its conduction band energy level is mainly contributed by Cd p orbitals, and its valence band energy level is mainly contributed by Cd d and S p orbitals. The direct band gap property allows it to produce photo-generated electron leaps without the action of additional kinetic energy when excited by light. Fig. 10e-f show the energy band structure and density of states diagrams of CoS₂. Staggered energy levels can be seen at its Fermi energy level, which indicates that it is a semimetallic catalyst. This property confers strong electrical conductivity and electron attraction ability, which can serve as an effective active site for hydrogen production to accelerate the separation of photogenerated carriers. As shown in Fig. 10g-j, the work function of CdS (002), CdS (100) and CdS (101) are 6.11 eV, 5.21 eV and 4.50 eV respectively. Larger work functions represent stronger electron binding ability, and more surface charges are effectively used to participate in H⁺ reduction reaction. In addition, the work function of CoS₂ (200) is 4.00 eV, and this difference in work function is the driving force for the change in potential difference between semiconductors and is necessary for the formation of heterojunctions [43]. In summary, theoretical calculations have determined that CdS (002) is a highly reactive hydrogen evolution crystalline surface, and the conditions for the formation of heterojunctions between CdS and CoS₂ are available.

3.6. Photocatalytic mechanism

The Mott-Schottky curve can be used to study the flat-band potential of the semiconductor (Fig. 11a-b). The flat band potential of CdS-L, CdS-P and CdS-R became more and more negative, which were -0.55 V, -0.62 V and -0.75 V, respectively, saturated calomel electrode as reference. Thus, their flat-band potentials at normal hydrogen electrode

are -0.31 V, -0.38 V and -0.51 V, respectively. According to the empirical conditions [44], the conduction band potential of n-type semiconductor is more negative than that of flat band by 0.2 V [45], and the conduction potential of CdS-R, CdS-P and CdS-L are -0.71 V, -0.58 V and -0.51 V respectively. Similarly, the conduction band potential for CoS₂ is -0.86 V. Fig. S4 displays the flat-band potential of each catalyst at different frequencies, and it can be observed that each set of data intersects at the same point.

Ultraviolet photoelectron spectroscopy (UPS) provides a more accurate understanding of the work function and energy level properties of semiconductors. As shown in Fig. 11c-f, the secondary electron cutoff energies of 18.33 eV, 18.15 eV, 17.74 eV and 18.45 eV were obtained for CdS-R, CdS-P, CdS-L and CoS₂, respectively, with He I (21.22 eV) as the excitation source [46]. The resulting work functions of CdS-R, CdS-P, CdS-L, CoS₂ are 2.89 eV, 3.07 eV, 3.49 eV, 2.78 eV, respectively. The larger work function gives the semiconductor a stronger electron-binding capability. In addition, the valence band values (vacuum) of CdS-R, CdS-P, CdS-L, CoS₂ are 6.05 V, 5.99 V, 6.24 V, and 5.36 V, respectively, based on their injection barriers (the difference between the Fermi energy level and the top of the valence band) [47]. Since the difference between the vacuum energy level and the normal hydrogen electrode is 4.44 V, their conduction and valence bands at the normal hydrogen electrode can be obtained by combining the optical band gaps, as shown in the Table 3. Fig. 12 visualizes the energy level relationship diagram of each catalyst.

Using Electron Paramagnetic Resonance (EPR) to capture free radicals can study the redox ability of the catalyst, which reflects the change

Table 3

The conduction band and valence band and forbidden band width parameters of catalysts.

Sample	ϕ	E_g	E_{CB}	E_{VB}
CdS-R	2.89 eV	2.36 eV	-0.75 V	1.61 V
CdS-P	3.07 eV	2.15 eV	-0.60 V	1.55 V
CdS-L	3.49 eV	2.35 eV	-0.55 V	1.80 V
CoS ₂	2.78 eV	1.88 eV	-0.96 V	0.92 V

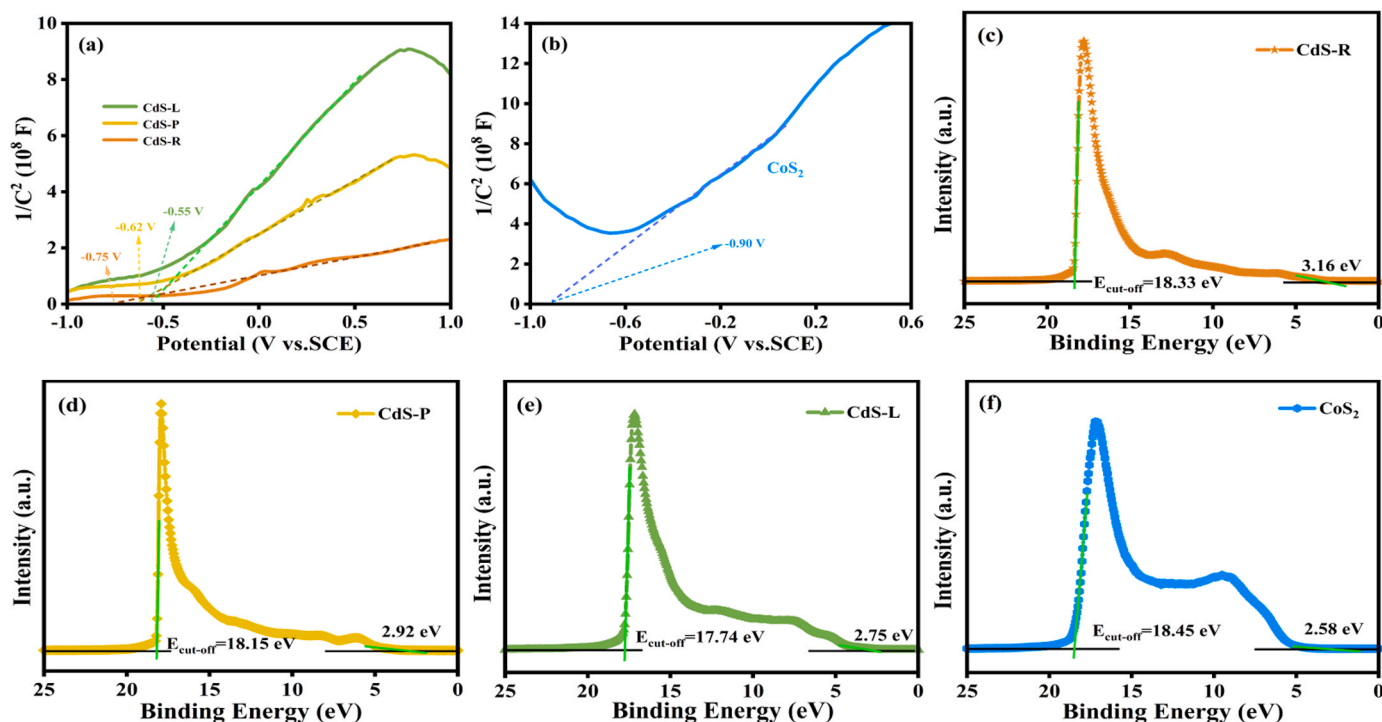


Fig. 11. Mott-schottky curves of CdS-x (x = R, P, L) (a) and CoS₂ (b); UPS curves of CdS-R (c), CdS-P (d), CdS-L (e) and CoS₂ (f).

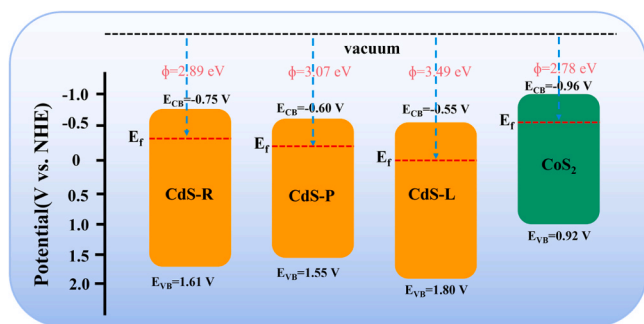


Fig. 12. Diagram of energy band structure and work function of CdS-R, CdS-P, CdS-L and CoS₂.

of redox ability after the formation of S-scheme heterojunction. As shown in Fig. 13a, CoS₂, CdS-L and 15CC-L did not show DMPO-·OH signals under light and dark conditions, because none of them reached the oxidation potential of OH[·]/OH (+1.99 V). Fig. 13b is the DMPO-·O₂ signal of each catalyst, and no signal was generated under dark conditions. The conduction bands of CoS₂, CdS-L and 15CC-L are all more negative than O₂/O₂^{·-} (-0.33 V). After irradiation, they all show DMPO-·O₂ signals, indicating that the catalysts are excited to generate photo-generated electrons. The DMPO-·O₂ signal of 15CC-L is stronger than that of CdS-L and CoS₂, indicating that the formation of S-scheme heterojunction brings stronger reducing ability to the composite catalyst, which is also a characteristic of S-scheme heterojunction. Fig. 13c shows the difference in reducing ability between 15CC-L and 15CC-R, and 15CC-L has a higher reducing ability because of its larger barrier height difference. In situ illumination X-ray photoelectron spectroscopy is an effective method to demonstrate the charge transfer direction of composite catalysts [48,49]. The fine XPS spectra of 15CC-L were tested in the dark and in the light, as shown in Fig. 13d-e, respectively. It can be seen that the binding energy corresponding to Cd 3d increases and that

corresponding to Co 3d decreases after illumination, which indicates the charge transfer from CdS to CoS₂ during the photocatalytic reaction [50]. The above analysis provides evidence for the S-scheme heterojunction mechanism of the composite catalyst 15CC-L [51].

After the above analysis, it was demonstrated that CdS-L has a more exposed and highly active (002) crystalline surface, showing a surprising hydrogen production activity. In addition to this, the composite photocatalyst was optimized according to its properties. The charge transfer direction of the composite catalyst under illumination was determined based on in situ XPS tests and free radical trapping experiments. The differences in work functions and energy bands provide the basic conditions and driving forces for the possible heterojunctions between them [52]. The energy level structure analysis shows that CdS-L has two advantages over CdS-R and CdS-P. First, the conduction band of CdS-L is closer to CoS₂, which makes the electrons on the conduction band of CdS-L more favorable for binding to the holes on the valence band of CoS₂ compared to the other two. Second, CdS-L and CoS₂ have a larger contact potential between them, which provides an additional fixation for the S-scheme heterojunction charge transfer pathway. An S-scheme heterojunction photocatalytic hydrogen production mechanism is proposed as shown in Fig. 14. Due to the difference in Fermi energy levels, the electron transfer on CoS₂ to CdS upon contact between the two leads to the formation of the built-in electric field and energy band bending. It is noteworthy that a larger contact potential barrier height ($E_{BH} = \phi_2 - \phi_1$) is generated between CdS-L and CoS₂ [53]. In photocatalytic hydrogen production, there are three driving forces for conventional S-scheme heterojunctions: the built-in electric field, energy band bending, and Coulomb forces [54,55]. Compared with CdS-R and CdS-P, the conduction band of CdS-L is closer to the valence band of CoS₂, which accelerates the complexation of unwanted photogenerated electrons and photogenerated holes. Meanwhile, the larger contact potential ($E_{BH3} > E_{BH2} > E_{BH1}$) is also able to effectively prevent the transfer of electrons from the CoS₂ conduction band to CdS-L as a function of yet another enhancement of the above action. The CoS₂

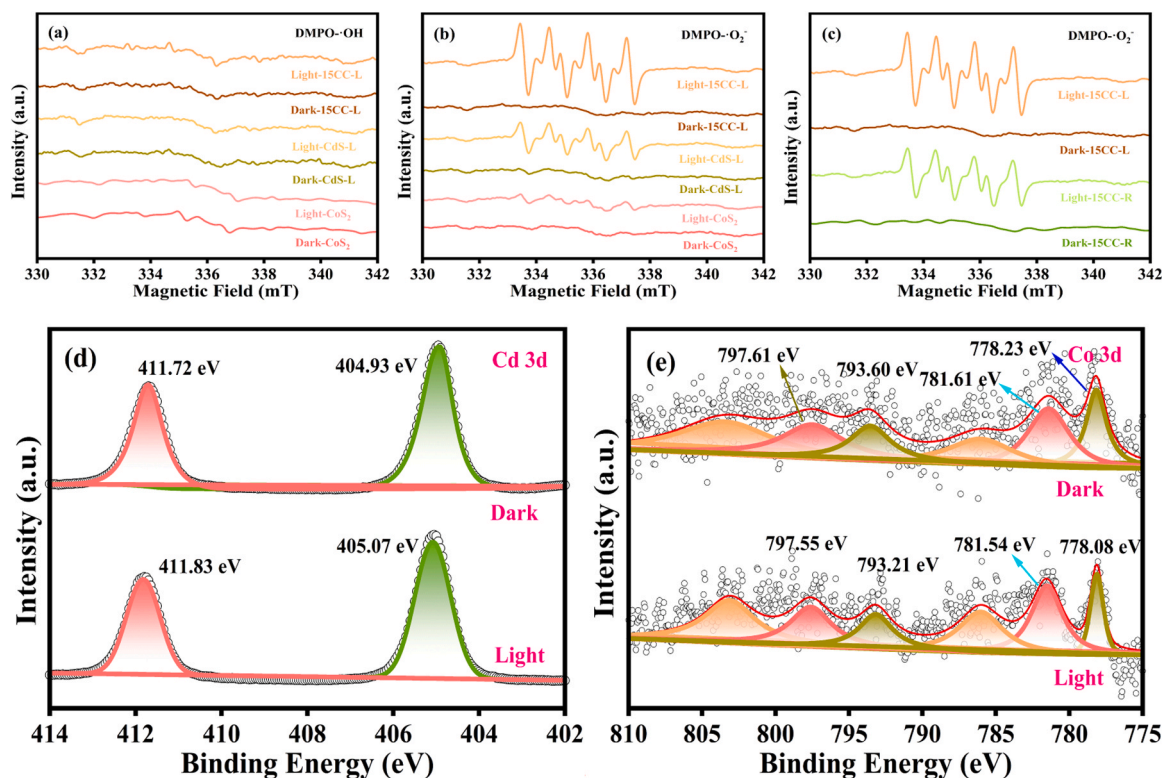


Fig. 13. EPR signal of ·OH of each catalyst (a); EPR signal of ·O₂ of each catalyst (b, c); Cd 3d (d) and Co 3d (e) XPS fine spectrum of 15CC-L at dark and light; Cd 3d (d) and Co 3d (e) XPS fine spectrum of 15CC-L at dark and light.

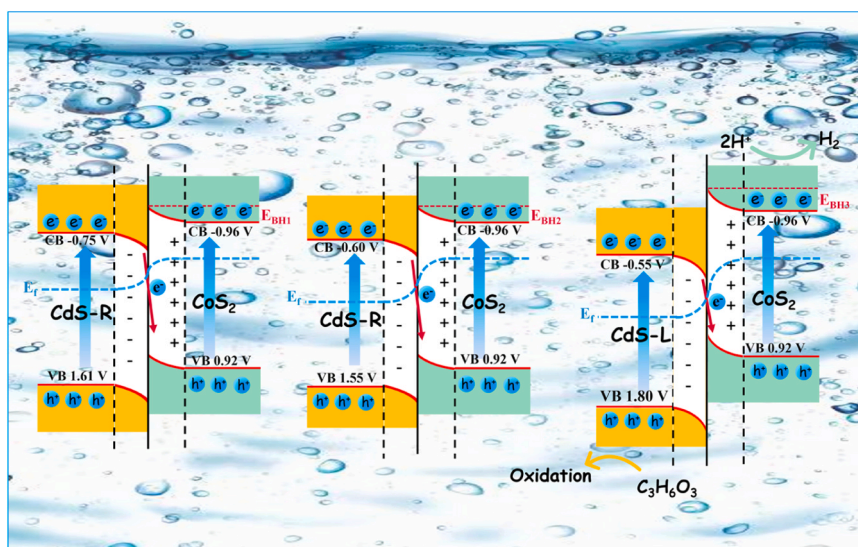


Fig. 14. Photocatalytic hydrogen evolution mechanism diagram of S-scheme heterojunction.

semimetallic properties make it a powerful electron-pulling effect as an active site. Therefore, this optimized system strengthens the inherent driving force of the conventional S-scheme heterojunction and produces a more significant hydrogen production effect.

4. Conclusion

The highly active hydrogen precipitation crystalline surface of CdS was determined by the density functional theory. The highly (002) crystalline exposed CdS was obtained by adjusting the preparation scheme, and S-scheme heterojunctions were constructed with CoS₂ nanoparticles. XRD, SAED analysis proved the successful preparation of high crystallinity single crystal CdS. Under 5 W white light irradiation, the single-crystal CdS-L exhibited a surprising hydrogen evolution activity (5.98 mmol·g⁻¹·h⁻¹), which was 3.49 times higher than that of CdS-L (1.71 mmol·g⁻¹·h⁻¹), and the composite photocatalyst CoS₂/CdS-L achieved a hydrogen production rate of 19.22 mmol·g⁻¹·h⁻¹. The work function and energy band positions of the catalysts were obtained by UV-vis DRS and UPS analyses, which are necessary for the construction and analysis of augmentative S-scheme heterojunctions. Meanwhile, carrier transfer experiments provide direct evidence for the charge transfer of S-scheme heterojunction photocatalytic mechanism.

CRedit authorship contribution statement

Xuanpu Wang: Methodology, Formal analysis, Investigation, Writing. **Zhiliang Jin:** Resources, Supervision, Funding acquisition.

Declaration of Competing Interest

The authors declare that they have no competing interests.

Data availability

Data will be made available on request.

Acknowledgements

This work was financially supported by the Natural Science Foundation of the Ningxia Hui Autonomous Region (2023AAC02046).

Appendix A. Supporting information

Supplementary data associated with this article can be found in the online version at doi:10.1016/j.apcatb.2023.123373.

References

- [1] Y. Liu, X. Hao, H. Hu, Z. Jin, High efficiency electron transfer realized over NiS₂/MoSe₂ S-scheme heterojunction in photocatalytic hydrogen evolution, *Acta Phys. Chim. Sin.* 37 (2021), 2008030.
- [2] Z. Jin, Application of graphdiyne in photocatalysis, *J. Chin. Ceram. Soc.* 51 (2023) 106–116.
- [3] C. Cheng, L. Mao, X. Kang, C. Dong, Y. Huang, S. Shen, J. Shi, L. Guo, A high-cyan groups-content amorphous-crystalline carbon nitride isotype heterojunction photocatalyst for high-quantum-yield H₂ production and enhanced CO₂ reduction, *Appl. Catal. B Environ.* 331 (2023), 122733.
- [4] Z. Jin, H. Li, J. Li, Efficient photocatalytic hydrogen evolution over graphdiyne boosted with a cobalt sulfide formed S-scheme heterojunction, *Chin. J. Catal.* 43 (2022) 303–315.
- [5] Z. Jin, Y. Wu, Novel preparation strategy of graphdiyne (C₈H₂N₂): one-pot conjugation and S-Scheme heterojunctions formed with MoP characterized with in situ XPS for efficiently photocatalytic hydrogen evolution, *Appl. Catal. B Environ.* 327 (2023), 122461.
- [6] T. Yan, X. Zhang, H. Liu, Z. Jin, CeO₂ particles anchored to ni2p nanoplate for efficient photo-catalytic hydrogen evolution, *Chin. J. Struct. Chem.* 41 (2022) 2201047–2201053.
- [7] H. Liu, Y. Zhang, Y. Li, M. Yang, Y. Li, Z. Jin, Mo-N bonds effect between MoS_x coupling with CoN for efficient photocatalytic hydrogen production, *ChemCatChem* 14 (2022), e202200413.
- [8] Y. Li, Z. Jin, X. Hao, Ni, Co-based selenide anchored g-C₃N₄ for boosting photocatalytic hydrogen, *Evol., Acta Phys. Chim. Sin.* 37 (2021), 1912033.
- [9] Y. Wu, Y. Li, L. Zhang, Z. Jin, NiAl-LDH in-situ derived Ni₂P and ZnCdS nanoparticles ingeniously constructed S-scheme heterojunction for photocatalytic hydrogen evolution, *ChemCatChem* 14 (2022), e202101656.
- [10] L. Zhang, Y. Wu, N. Tsubaki, Z. Jin, 2D/3D S-scheme heterojunction interface of CeO₂-Cu₂O promotes ordered charge transfer for efficient photocatalytic hydrogen evolution, *Acta Phys. Chim. Sin.* 39 (2023), 2302051.
- [11] X. Wang, Z. Jin, X. Li, Monoclinic β-AgVO₃ coupled with CdS formed a 1D/1D p-n heterojunction for efficient photocatalytic hydrogen evolution, *Rare Met.* (2023), <https://doi.org/10.1007/s12598-022-02183-y>.
- [12] J. Li, M. Li, Y. Li, X. Guo, Z. Jin, Lotus-leaf-like Bi₂O₃CO₃ nanosheet combined with Mo₂S₃ for higher photocatalytic hydrogen evolution, *Sep. Purif. Technol.* 288 (2022), 120588.
- [13] X. Li, Y. Li, X. Guo, Z. Jin, Design and synthesis of ZnCo₂O₄/CdS for substantially improved photocatalytic hydrogen production, *Front. Chem. Sci. Eng.* (2023), <https://doi.org/10.1007/s11705-022-2233-4>.
- [14] L. Zhang, X. Hao, J. Li, Y. Wang, Z. Jin, Unique synergistic effects of ZIF-9(Co)-derived cobalt phosphide and CeVO₄ heterojunction for efficient hydrogen evolution, *Chin. J. Catal.* 41 (2020) 82–94.
- [15] C. Liu, J. Zuo, J. Zhang, Y. Pei, S. Chen, Exploring the effects of crystal facet orientation at the heterojunction interface on charge separation for photoanodes, *ACS Appl. Mater. Interfaces* 15 (2023) 3566–3573.

- [16] J. Zhang, Y. Song, X. Dong, H. Jiang, J. Tang, H. Li, Umbrella-like CdS single crystal: exposed (002) facets and enhanced photocatalytic properties, *J. Mater. Sci.* 55 (2020) 11167–11176.
- [17] D. Yan, Z. Xue, F. Chen, X. Liu, Z. Yang, Y. Pei, S. Zhou, C. Zhao, Exposed (002) facets and controllable thickness of CdS nanobelts drive desirable hydrogen-adsorption free energy (ΔG_H) for boosting visible-light photocatalytic performance, *Catal. Sci. Technol.* 11 (2021) 7486–7492.
- [18] L. Wu, Q. Wang, T. Zhuang, Y. Li, G. Zhang, G. Liu, F. Fan, L. Shi, S. Yu, Single crystalline quaternary sulfide nanobelts for efficient solar-to-hydrogen conversion, *Nat. Commun.* 11 (2020) 5194.
- [19] Y. Dong, X. Fei, Z. Liu, Y. Zhou, L. Cao, Synthesis and photocatalytic redox properties of anatase TiO₂ single crystals, *Appl. Surf. Sci.* 394 (2017) 386–393.
- [20] H. Yin, J. Zhang, Y. Wang, X. Zhao, Y. Qu, Y. Peng, H. Li, Y. Huo, J. Li, Alloying effect of PdCu-TiO₂ in photocatalytic membrane reactor for efficient removal of humic acid foulant, *Appl. Catal. B Environ.* 338 (2023), 123085.
- [21] Y. Cao, H. Gou, P. Zhu, Z. Jin, Ingenious design of CoAl-LDH p-n heterojunction based on CuI as holes receptor for photocatalytic hydrogen evolution, *Chin. J. Struct. Chem.* 41 (2022) 2206079–2206085.
- [22] X. Wang, Y. Li, T. Li, Z. Jin, Synergistic effect of bimetallic sulfide enhances the performance of CdS photocatalytic hydrogen evolution, *Adv. Sustain. Syst.* 7 (2023), 2200139.
- [23] Z. Jin, T. Li, L. Zhang, X. Wang, G. Wang, X. Hao, Construction of a tandem S-scheme GDY/CuI/CdS-R heterostructure based on morphology-regulated graphdiyne ($g-C_6H_{2n-2}$) for enhanced photocatalytic hydrogen evolution, *J. Mater. Chem. A* 10 (2022) 1976–1991.
- [24] Y. Dang, L. Luo, W. Wang, W. Hu, X. Wen, K. Lin, B. Ma, Improving the photocatalytic H₂ evolution of CdS by adjusting the (002) crystal facet, *J. Phys. Chem. C* 126 (2022) 1346–1355.
- [25] C. Li, L. Han, R. Liu, H. Li, S. Zhang, G. Zhang, Controlled synthesis of CdS micro/nano leaves with (0001) facets exposed: enhanced photocatalytic activity toward hydrogen evolution, *J. Mater. Chem.* 22 (2012) 23815.
- [26] B. Ng, L. Putri, X. Kong, K. Shak, P. Pasbakhsh, S. Chai, A. Mohamed, Sub-2nm Pt-decorated Zn_{0.5}Cd_{0.5}S nanocrystals with twin-induced homojunctions for efficient visible-light-driven photocatalytic H₂ evolution, *Appl. Catal. B Environ.* 224 (2018) 360–367.
- [27] A. Jiang, H. Guo, S. Yu, F. Zhang, T. Shuai, Y. Ke, P. Yang, Y. Zhou, Dual charge-accepting engineering modified AgInS₂/CdS quantum dots for efficient photocatalytic hydrogen evolution overall H₂S splitting, *Appl. Catal. B Environ.* 332 (2023), 122747.
- [28] G. Zhang, S. Huang, X. Li, D. Chen, N. Li, Q. Xu, H. Li, J. Lu, Internal electric field engineering of bifunctional 2D/2D heterojunction photocatalyst for cooperative H₂ production and alcohol conversion, *Appl. Catal. B Environ.* 331 (2023), 122725.
- [29] Q. Zhu, B. Qiu, H. Duan, Y. Gong, Z. Qin, B. Shen, M. Xing, J. Zhang, Electron directed migration cooperated with thermodynamic regulation over bimetallic NiFeP/g-C₃N₄ for enhanced photocatalytic hydrogen evolution, *Appl. Catal. B Environ.* 259 (2019), 118078.
- [30] Z. Yang, M. Li, S. Chen, S. Yang, F. Peng, J. Liao, Y. Fang, S. Zhang, S. Zhang, Cocatalyst engineering with robust tunable carbon-encapsulated Mo-rich Mo/Mo₂C heterostructure nanoparticle for efficient photocatalytic hydrogen evolution, *Adv. Funct. Mater.* 33 (2023), 2212746.
- [31] Z. Fan, X. Guo, M. Yang, Z. Jin, Mechanochemically preparation and application of graphdiyne coupled with CdSe nanoparticles for efficient photocatalytic hydrogen production, *Chin. J. Catal.* 43 (2022) 2708–2719.
- [32] G. Wang, Y. Quan, K. Yang, Z. Jin, EDA-assisted synthesis of multifunctional snowflake-Cu₂S/CdZnS S-Scheme heterojunction for improved the photocatalytic hydrogen evolution, *J. Mater. Sci. Technol.* 121 (2022) 28–39.
- [33] Y. Shao, X. Hao, Z. Jin, Construction of double S-scheme ZIF-67@GDY/CuI heterojunction by graphdiyne ($g-C_6H_{2n-2}$) nanosheets-coated ZIF-67 on synergized charge transfer for enhanced photocatalytic hydrogen, *Evol., Sol. RRL* 7 (2023), 2201054.
- [34] Z. Lian, F. Wu, Y. Zhong, J. Zi, Z. Li, X. Wang, T. Nakagawa, H. Li, M. Sakamoto, Tuning plasmonic p-n junction for efficient infrared-light-responsive hydrogen evolution, *Appl. Catal. B Environ.* 318 (2022), 121860.
- [35] Z. Lian, F. Wu, J. Zi, G. Li, W. Wang, H. Li, Infrared light-induced anomalous defect-mediated plasmonic hot electron transfer for enhanced photocatalytic hydrogen evolution, *J. Am. Chem. Soc.* 145 (2023) 15482–15487.
- [36] Z. Jin, X. Wang, In situ XPS proved efficient charge transfer and ion adsorption of ZnCo₂O₄/CoS S-Scheme heterojunctions for photocatalytic hydrogen evolution, *Mater. Today Energy* 30 (2022), 101164.
- [37] T. Yan, H. Liu, Z. Jin, Graphdiyne based ternary GD-CuI-NiTiO₃ S-scheme heterojunction photocatalyst for hydrogen evolution, *ACS Appl. Mater. Interfaces* 13 (2021) 24896–24906.
- [38] T. Li, Y. Li, Z. Jin, Surface-induced engineering: P-induced formation of surface bonding states based on the ZIF synthesis strategy for photocatalytic hydrogen evolution, *Inorg. Chem.* 61 (2022) 12809–12821.
- [39] Z. Jin, X. Wang, Y. Wu, T. Li, Graphdiyne (C_6H_{2n-2}) based S-scheme heterojunction to promote carrier transfer for efficiently photocatalytic hydrogen evolution, *2D Mater.* 10 (2023), 025022.
- [40] X. Wang, T. Li, X. Wang, Z. Jin, A novel graphdiyne (C_6H_{2n-2}) synthesis strategy: design and application of an organic/inorganic conjugated system for photocatalytic hydrogen production, *J. Mater. Chem. C* 11 (2023) 1798–1811.
- [41] T. Li, Z. Jin, Rationally engineered active sites for efficient and durable hydrogen production over γ -graphyne assembly CuMoO₄ S-scheme heterojunction, *J. Catal.* 417 (2023) 274–285.
- [42] W. Li, F. Wang, X. Liu, Y. Dang, J. Li, T. Ma, C. Wang, Promoting body carriers migration of CdS nanocatalyst by N-doping for improved hydrogen production under simulated sunlight irradiation, *Appl. Catal. B Environ.* 313 (2022), 121470.
- [43] X. Ruan, C. Huang, H. Cheng, Z. Zhang, Y. Cui, Z. Li, T. Xie, K. Ba, H. Zhang, L. Zhang, X. Zhao, J. Leng, S. Jin, W. Zhang, W. Zheng, S.K. Ravi, Z. Jiang, X. Cui, J. Yu, A. Twin, S-scheme artificial photosynthetic system with self-assembled heterojunctions yields superior photocatalytic hydrogen evolution rate, *Adv. Mater.* 35 (2023), 2209141.
- [44] H. Liu, Y. Zhang, D. Li, Y. Li, Z. Jin, Design and preparation of a CeVO₄/Zn_{0.5}Cd_{0.5}S S-scheme heterojunction for efficient photocatalytic hydrogen evolution, *ACS Appl. Energy Mater.* 5 (2022) 2474–2483.
- [45] W. Li, X. Wang, Q. Ma, F. Wang, X. Chu, X. Wang, C. Wang, CdS@h-BN heterointerface construction on reduced graphene oxide nanosheets for hydrogen production, *Appl. Catal. B Environ.* 284 (2021), 119688.
- [46] Y. Hou, X. Du, S. Scheiner, D.P. McMeekin, Z. Wang, N. Li, M.S. Killian, H. Chen, M. Richter, I. Levchuk, N. Schrenker, E. Spiecker, T. Stubhan, N.A. Luechinger, A. Hirsch, P. Schmuki, H.-P. Steinrück, R.H. Fink, M. Halik, H.J. Snaith, C. J. Brabec, A generic interface to reduce the efficiency-stability-cost gap of perovskite solar cells, *Science* 358 (2017) 1192–1197.
- [47] R. Shen, X. Lu, Q. Zheng, Q. Chen, Y.H. Ng, P. Zhang, X. Li, Tracking S-scheme charge transfer pathways in Mo₂C/CdS H₂-evolution photocatalysts, *Sol. RRL* 5 (2021), 2100177.
- [48] Z. Wang, B. Cheng, L. Zhang, J. Yu, H. Tan, BiOBr/NiO S-scheme heterojunction photocatalyst for CO₂ photoreduction, *Sol. RRL* 6 (2022), 2100587.
- [49] T. Wang, Z. Jin, Graphdiyne (C_6H_{2n-2}) based CuI-GDY/ZnAl LDH double S-scheme heterojunction proved with in situ XPS for efficient photocatalytic hydrogen production, *J. Mater. Sci. Technol.* 155 (2023) 132–141.
- [50] H. Ren, F. Qi, A. Labidi, J. Zhao, H. Wang, Y. Xin, J. Luo, C. Wang, Chemically bonded carbon quantum dots/Bi₂WO₆ S-scheme heterojunction for boosted photocatalytic antibiotic degradation: Interfacial engineering and mechanism insight, *Appl. Catal. B Environ.* 330 (2023), 122587.
- [51] Y. Yang, B. Cheng, J. Yu, L. Wang, W. Ho, TiO₂/In₂S₃ S-scheme photocatalyst with enhanced H₂O₂-production activity, *Nano Res.* 16 (2023) 4506–4514.
- [52] H. Li, H. Gong, Z. Jin, In₂O₃-modified Three-dimensional nanoflower MoS_x form S-scheme heterojunction for efficient hydrogen production, *Acta Phys. Chim. Sin.* 38 (2022), 2201037.
- [53] C. Cheng, J. Zhang, R. Zeng, F. Xing, C. Huang, Schottky barrier tuning via surface plasmon and vacancies for enhanced photocatalytic H₂ evolution in seawater, *Appl. Catal. B Environ.* 310 (2022), 121321.
- [54] L. Zhang, J. Zhang, H. Yu, J. Yu, Emerging S-scheme photocatalyst, *Adv. Mater.* 34 (2022), 2107668.
- [55] T. Li, N. Tsubaki, Z. Jin, S-scheme heterojunction in photocatalytic hydrogen production, *J. Mater. Sci. Technol.* 169 (10) (2023) 82–104.